3D printing of ABS Nanocomposites. Comparison of processing and effects of multi-wall and single-wall carbon nanotubes on thermal, mechanical and electrical properties

Sithiprumnea Dul [a,*], Brenda J. Alonso Gutierrez [b,c], Alessandro Pegoretti [a], Jaime Alvarez-Quintana [b], Luca Fambri [a,*]

[a] *Department of Industrial Engineering and INSTM Research Unit, University of Trento, Trento 38123, Italy*
[b] *Centro de Investigación en, Materiales Avanzados S. C. Unidad Monterrey, Apodaca 66600, Mexico*
[c] *Facultad de Ingeniería Mecánica y Eléctrica, Universidad Autónoma de Nuevo León, Avenida Universidad s/n, Ciudad Universitaria, San Nicolás de los Garza 66451, México*

ARTICLE INFO

ABSTRACT

The following paper reports on a comparative study of the effects of two types of carbon nanotubes, namely multiwall (MWCNT) and single-wall (SWCNT) carbon nanotube, on the properties of 3D-printed parts produced with acrylonitrile-butadiene-styrene (ABS) nanocomposites with various CNT loadings of 5-10 wt.%. Quasi-static tensile properties and Vicat softening temperature of 3D-printed parts were enhanced with the increasing CNT content. The highest enhancement in tensile properties was observed for the ABS/CNT nanocomposites at 10 wt.% filler loading. 3D-printed ABS/SWCNT composites showed higher tensile modulus, better creep stability and higher Vicat temperature. However, the strength of ABS/SWCNT 3D samples is relatively lower than that of ABS/MWCNT. In addition, 3D-printed parts exhibited anisotropic electrical conductive behaviour, which has a conductivity of through-layer of about 2-3 orders of magnitude higher than cross-layer. The highest conductivity of 3D-printed samples reached 25.2 S/m, and 9.3 S/m for ABS/MWCNT and ABS/SWCNT composites at 10 wt.%, respectively. The results obtained, i.e. the successful fuse filament fabrication and the consequent electromechanical properties, confirm that these 3D printable nanocomposite could be properly utilized for the production, and application up to about 90°C, of thermoelectric devices and/or resistors for flexible circuits.

© 2022 Published by Elsevier Ltd on behalf of The editorial office of Journal of Materials Science & Technology.

1. Introduction

Three-dimensional (3D) printing (also known as additive manufacturing) is a prominent manufacturing technology with recent developments and applications in the industry and academia. The 3D object is manufactured by stacking materials from various possible forms of liquid, powder or sheets layers by layers, according to 3D model data [1]. The advantages of 3D printing are not limited to the possibility of manufacturing a final part without using auxiliary tool/molds, but they also represent viable solutions for the fabrications of complex-shaped parts that are challenging to be manufactured by conventional methods. Therefore, this technology also has substantial benefits over removal or subtractive manufacturing methodologies because of almost neglectable waste material

generated, as in the case of supports or brims and skirt residue. Up to now, additive manufacturing can meet the development requirements for customized products and prototypes and also for relatively low-volume end-use productions.

Seven categories of additive manufacturing technologies have been classified by ASTM Committee F42, namely materials extrusion, powder bed fusion, vat photopolymerization, binder jetting, materials jetting, sheet lamination and directed energy deposition. In the subgroup of materials extrusion, fused filament fabrication (FFF) represents a popular choice among 3D printing methods, thanks to their advantages of simplicity, low cost, reduced waste and easy replacement of materials. In the FFF process, a thermoplastic-based filament is heated in a chamber at a temperature above the glass transition for amorphous polymers (about 100-150°C) or above melting temperatures for semicrystalline polymers (about 20-30°C) and deposited through a nozzle on an XY platform to build a 3D object. The FFF parameters, which can affect the performance of the 3D-printed parts, are printing
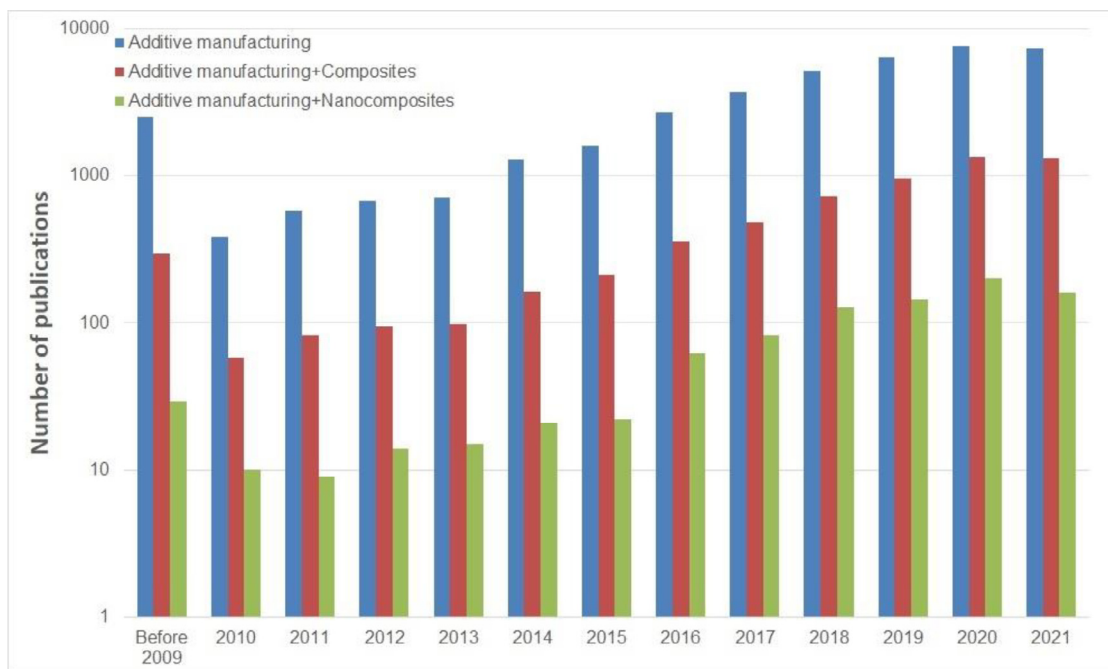
Fig. 1. Number of publications in the field of additive manufacturing and its integration with composites and nanocomposites from Web of Science™ in the last decade (up to October 30th, 2021).

temperature (at nozzle, bed and printing environment), build orientation, layer height, infill pattern and density [2,3]. Moreover, the role of the selected filler in FFF of nanocomposites should be properly considered because it could significantly affect the overall process (rheology, heating-cooling rate, and crystallization, ...) and, consequently the final properties of the manufacture.

In the last decade, the development of novel polymeric formulations compatible with additive manufacturing has become one of the most popular research topics. Integration of two developing research areas of polymer nanocomposites and additive manufacturing (AM) can offer mutual benefits, as documented by the growing number of publications indicated in Fig. 1. Polymer nanocomposites (PNCs) are usually obtained through the dispersion of nanofillers in polymeric matrices to fabricate multifunctional properties, such as mechanical stiffness and strength, electrical, thermal conductivities, magnetism, and electro-mechanical sensitivity. Indeed, an AM technique offers the opportunity to manufacture products with highly complex geometry, shorter manufacturing time and less tooling. The new polymer nanocomposites can lead to lightweight structural materials with functionalities that further expand their applications, such as in electronic components [4,5], micro-batteries [6], circuits [7] and electromagnetic shielding [8].

Carbonaceous nanofillers (e.g., carbon nanotubes, graphene and carbon black) were incorporated in various polymeric matrices such as polylactic acid (PLA) [9–11], polyamide [12], thermoplastic polyurethanes (TPU) [13], ABS [2] and epoxy [14–16]. Their performance, including mechanical properties and the thermal and electrical conductivities of double-filler nanocomposites, has been shown to be higher than that of single-filler nanocomposites, probably due to synergistic effects from both fillers. Other works on hybrid carbon nanotube (CNT)/graphene nanoplatelets (GNP) for the fused filament fabrication (FFF) in different matrices, such as PLA [9-11,17] and poly-ether-ether-ketone (PEEK) [18] provided evidence that is possible to modulate the properties and, in some cases, find synergistic effects [19–21]. 3D-printed nanocomposites were also investigated in electrical and thermal conductivity, tribological properties and electromagnetic shielding behaviour.

Our group has begun research on carbonaceous ABS nanocomposite based on graphene and carbon nanotubes [2, 22 and references therein] with specific attention to the composite preparation via melt compounding and to the subsequent possibility of 3D printing (an additive manufacturing process in molten state). The amorphous copolymer matrix has been properly selected in order to achieve higher using temperatures of the resulting nanocomposites than PLA nanocomposites, as a direct consequence of their Tg (about 110°C for ABS, and about 60°C for PLA).

A more recent study of our research group focused on multi-walled (MWCNT) and single-walled carbon nanotube (SWCNT) dispersed in ABS matrix up to their maximum concentration of 10 wt.% through a solvent-free mixing process in order to produce ABS nanocomposite filaments [22]. The experimental study revealed that nanofillers showed an increase in modulus and tensile strength as well as a significant reduction of the strain at break. Specifically, ABS/SWCNT composite filaments exhibited significantly higher mechanical properties than ABS/MWCNT ones, probably due to the dispersion of SWCNTs into ABS matrix and a better orientation of the reinforcement. ABS/SWCNT nanocomposite filaments were also found to have slightly lower electrical resistivity than the corresponding ABS/MWCNT composition for 5-10 wt.%. In particular, a marked resistivity in the range 0.2-2.1 Ω cm was observed after the dispersion of CNT [22]. The choice of maximum 10 wt.% content appeared an appropriate compromise between nanocomposite 3D-processability and mechanical-electrical properties, as shown by previous research [23]. Indeed, Sezer and Eder showed a value of conductivity in the range of 10^{-3}-10^{-1} S/cm for ABS nanocomposites at 5-10 wt. % of MWCNT, almost irrespective of the raster angle [-45, 45] or [0, 90]. At the same time, they also reported critical problems during the 3D printing process of nanocomposite filaments at %10 loading for nozzle clogging.

In the current paper, we attempt to shed more light on the production process of 3D printing of ABS nanocomposites with SWCNT and MWCNT nanofillers up to 10 wt.%. In particular, mechanical properties and electrical behavior of the produced specimens were compared in order to highlight the potentialities

Table 1
Properties of commercial single-walled and multi-walled carbon nanotubes according to the manufacturer.

Nanoparticle	Manufacturer	Density (g/cm^3)	Length (μm)	Diameter (nm)	Aspect ratio	Surface area (m^2/g)	Carbon purity (%)
MWCNT-NC7000	Nanocyl, Belgium	2.15 $\pm$ 0.03*	1.5	9.5	158	250-300	>90
SWCNT-TUBALL	TUBALL, USA	1.877**	5	1.6 $\pm$ 0.4	3125	>300	>80

* from Ref [25].; ** from Ref [26]..
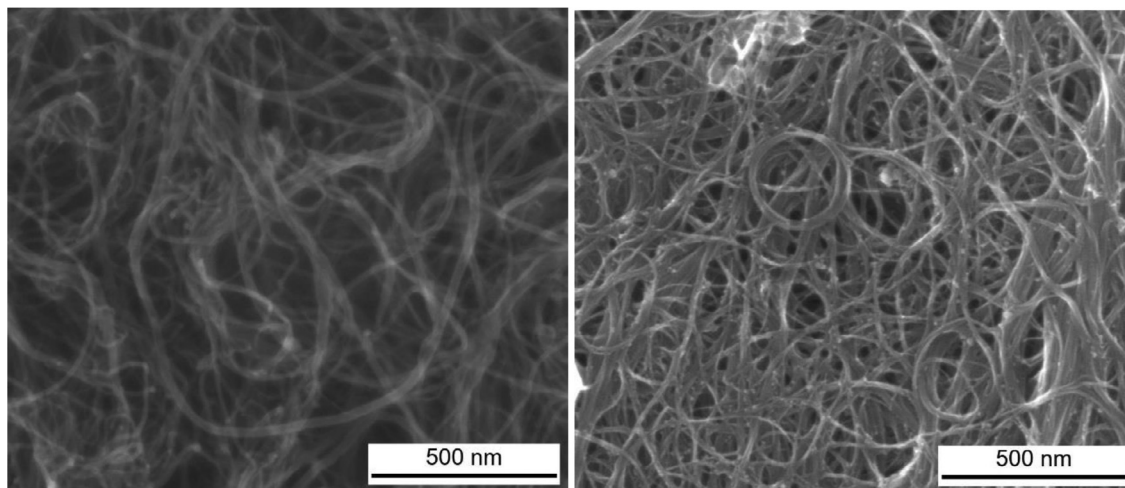
**Fig. 2.** SEM micrographs of MWCNT (a) and SWCNT (b).

of FFF techniques for specific applications of high conductivity materials.

2. Materials and methods

2.1. Materials

Acrylonitrile butadiene styrene (ABS) with tradename Sinkral® F322 was offered by Versalis S.p.A. (Mantova, Italy). According to the manufacturer's technical data sheet, the material has a density of 1.04 g/cm^3 and a melt flow rate of 14 cm^3/10 min (220°C/10 kg) [24]. Multi-wall (MW) and single-wall (SW) carbon nanotubes selected in this work are presented in Table 1, which reports the details of their sizes and physical properties, according to the producer datasheet.

The morphology of the two different CNTs, along with the evidence of various diameter nanotubes, is depicted in Fig. 2, from which it was possible to measure diameters in range of 10-25 nm for MWCNT (Fig. 2(a)) and observe that SWCNT (Fig. 2(b)) presented a diameter in the range of 7-20 nm. The latter is quite larger than that declared by the producers (some SWCNT of 3-4 nm were also measured). In a previous research on MWCNT nanocomposites, the external diameter of tubes was measured to be about 15-20 nm, and wall thickness of about 5 nm was also reported [27]. Moreover, the different MWCNT and SWCNT were also compared through Raman spectra, as reported **in** Fig. 3. MWCNT exhibited two medium intensity peaks at 1335 cm^{-1} (D Band), and at 1568 cm^{-1} (G Band), with a small shoulder at 1601 cm^{-1}, and a secondary peak at 2674 cm^{-1} (G' Band), as second harmonic of D band. On the other hand, a very intense peak (G band) at 1586 cm^{-1}, was shown by SWCNT with a shoulder at 1564 cm^{-1}, and secondary G' Band at 2667 cm^{-1}; other signals with minor intensity at 1333 cm^{-1} (D Band) and at 1734 cm^{-1} were also detected in SWCNT spectra. The different structure quality of CNT, Q_{CNT}, could be evaluated by the ratio of the intensities of the G and D bands $Q_{CNT} = (I_D/I_G)$. It is worth noting the lower quality of CNTs, $Q_{MWCNT} = 0.87$, about 100 times lower than SWCNT
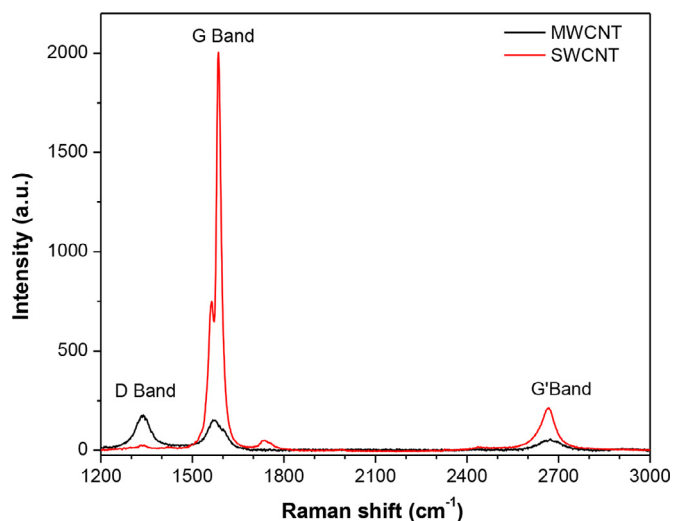
Fig. 3. Comparative Raman spectra of MWCNT and SWCNT.

($Q_{SWCNT} = 80.1$), as dependance of a structural damage and/or certain disorder in the crystal domains of multiwall carbon nanotubes. Those differences could affect the interaction with ABS matrix and the dispersion during nanocomposite preparation.

2.2. Material processing and sample preparation

2.2.1. Compounding and filament extrusion

Materials were dried at 80°C in a vacuum oven for at least 2 h before processing.

MWCNT and SWCNT nanofillers at a concentration of 5, 7.5 and 10 wt.% were melt compounded with ABS in Thermo-Haake Polylab Rheomix counter-rotating internal mixer (Thermo Haake, Karlsruhe, Germany) at 190°C (rotor speed of 90 rpm for 15 min). Batches of about 40-45 g were prepared for each composition. Af-
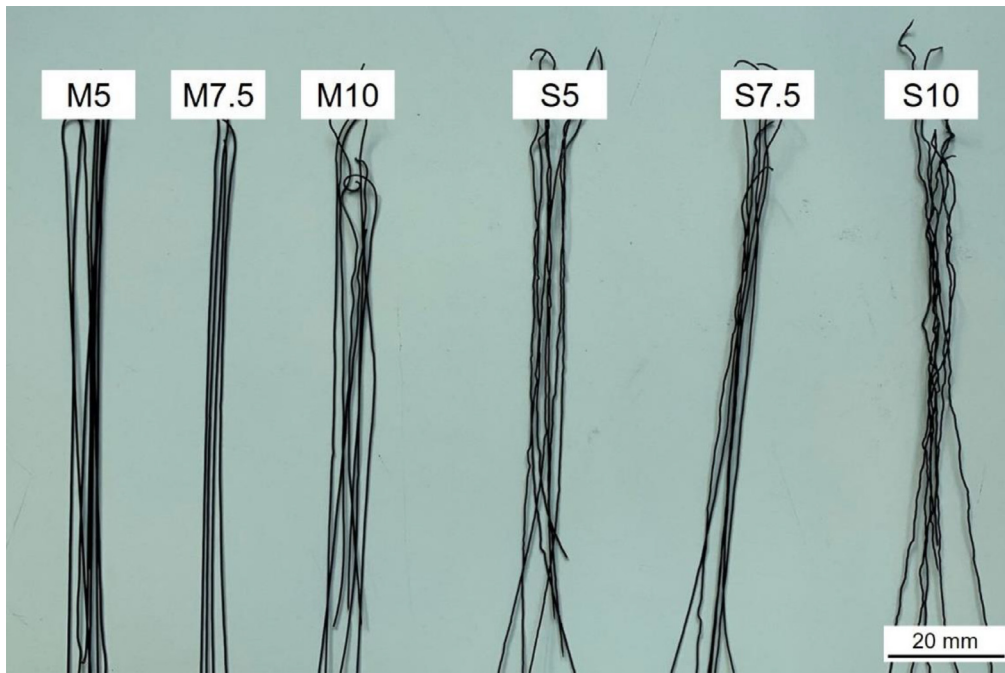
Fig. 4. ABS/MWCNT (M) and ABS/SWCNT (S) fibers at different wt.% CNT content, freely extruded from the nozzle of a 3D printer.

ter the mixing, all composites were milled into fine powder by a using grinder IKA M20 Universal mill (IKA®-Werke GmbH&Co. KG, Staufen, Germany). Nanocomposite filaments with a diameter of 1.75 ± 0.05 mm were produced by a single-screw extruder model Estru 13 (Friul Filiere SpA, Buia-UD, Italy), with a screw diameter of 14 mm; die diameter of 2 mm; temperature profile of the extruder 100-220°C; $T_4 = 230$°C (rod die); screw rotation 30 rpm (see details in literature [22]). Composition of nanocomposites was designated indicating the type of filler, MWCNT or SWCNT, as M or S respectively, and their relative weight percentage. For instance, M7.5 refers to nanocomposite composition of 7.5 wt.% MWCNT, while the unfilled matrix was denoted as ABS.

2.2.2. 3D-extruded fibers

3D-extruded fibers were produced by using a prototype of a 3D printer for high-temperature processing, Sharebot HT Next Generation desktop (Sharebot NG, Nibionno, LC, Italy) through a nozzle diameter of 0.40 mm at a temperature of 280°C starting from the extruded filament. Fibers of about 100 mm length were freely extruded, as shown in Fig. 4. Differently from ABS/MWCNT fibers, ABS/SWCNT fibers appeared curly, as a consequence of the shrinkage effects in free cooling, due to their lower viscosity and the higher orientation of CNT in the molten state. During the process of 3D-extrusion, the Feeding Orientation factor (OF_{Feed}), the Spinning Orientation factor (OF_{Spin}) and the Total Orientation factor (OF_{Tot}) were determined as relative ratio of the different sections, according to the equations

$$OF_{\text{Feed}} = (D_{\text{Fil}}/D_{\text{noz}})^2 \tag{1}$$

$$OF_{\text{Spin}} = (D_{\text{noz}}/D_{\text{fib}})^2 \tag{2}$$

$$OF_{\text{Tot}} = OF_{\text{Feed}} \times OF_{\text{Spin}} = (D_{\text{Fil}}/D_{\text{fib}})^2 \tag{3}$$

as function of the diameter of the filament (D_{Fil}), the nozzle ($D_{\text{noz}} = 400$ μm) and the fiber (D_{fib}), respectively. Moreover, the swelling ratio SW_{Spin} and the draw ratio DR_{Spin} in Spinning have been also calculated according to equations,

$$SW_{\text{Spin}} = 1/OF_{\text{Spin}} = (D_{\text{fib}}/D_{\text{noz}})^2 \tag{4}$$

$$DR_{\text{Spin}} = (D_{\text{fib}}/D_{\text{Ski}})^2 \tag{5}$$

where D_{Ski} is the equivalent diameter of the Skirt (see Fig. 5(b, c)).

2.2.3. 3D-Printing

The 3D-printed specimens were produced by a prototype Sharebot HT Next Generation desktop 3D printer (Sharebot NG, Nibionno, LC, Italy), which was adapted to temperatures up to 500°C. Specimens, as shown in Table 2, were 3D-printed by using filaments to feed the 3D-printer following printing parameters in Table 3.

A scheme of dumbell and parallelepid models according to the Slic3r software, and example of printed samples are shown in Fig. 5. Single layer is deposited along the plane XY, whereas Z direction represents the thickness of the sample obtained by the progressive overlapping of the required layers. Yellow lines represent two aligned fibers (contour), and green lines indicate the elements of Skirt (external frame) and Brim (around specimen). Red lines represent the infill with a raster angle of $\pm$ 45°; maximum fill percentage (100%). No raft was used. The nozzle speed for fiber deposition has been fixed at 40 mm/s

2.3. Testing techniques

2.3.1. Scanning electron microscopy (SEM) and Raman spectroscopy

Surface morphology of MWCNT and SWCNT was observed at high magnification by using a scanning electron microscope (SEM) model JEOL 6010 plus at an accelerating voltage of 15 kV.

Morphological analysis of 3D-printed samples was performed on the cross-section obtained by fragile fracture in liquid nitrogen, ten layers specimens were observed by a Carl Zeiss AG Supra 40 field-emission scanning electron microscope (FESEM) (Carl Zeiss AG, Oberkochen, Germany) at an acceleration voltage of 8-10 kV.

Raman spectra were obtained by using a Micro-RAMAN DXR Thermoscientific spectrometer (Thermo Scientific, Karlsruhe, Germany) equipped with an Ar+ ion laser excitation at a wavelength of 532 nm.

Table 2
Dimensions, geometrical parameters in production, and analysis of FFF specimens.

Samples	X (mm)	Y (mm)	Z (mm)	Deposition time of a single layer (sec)	Number of layers	Total time (min)	Analysis
Dumbbell 1	75	5-10[a]	2	145	10	24.2	Tensile
Dumbbell 2	75	5-10[a]	0.6	145	3	7.3	Creep
Dumbbell 3	75	5-10[a]	0.6	145	1	2.4	Resistivity
Parallelepiped	30	5	2	55	10	9.2	Density, VST and resistivity

[a] min and max width of Dumbbell specimen are reported.

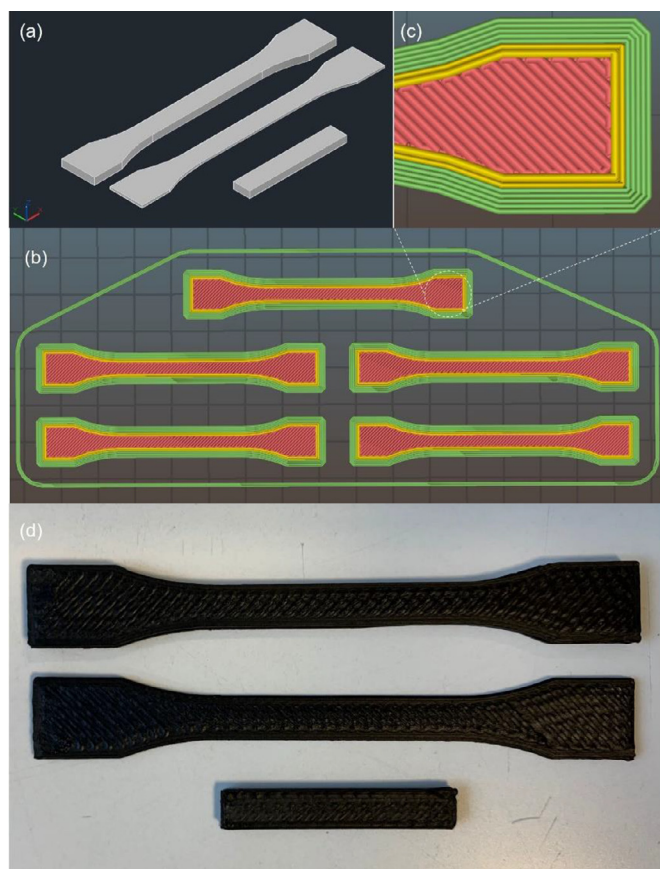**Fig. 5.** (a) 3D model of 1BA dumbbells (thickness of 2 mm and 0.6 mm) and plate (30 × 5 × 2 mm³), (b) the arrangement of dumbbells, (c) the detail of infill pattern [+45°/-45°] and (d) 3D-printed samples.

Table 3
3D printing parameters by fused filament fabrication technique for specimen's production.

Parameter	Value
Nozzle diameter	0.4 mm
Nozzle temperature	280°C
Bed temperature	110°C
Nozzle speed	40 mm/s
Layer height	0.2 mm
Raster angle	+45°/-45°
Infill density	100%
Number of contours	2

2.3.2. Density measurement

Density measurement of 3D-printed composites was performed on sheet samples (30 × 5 × 2 mm³) as the weight/volume ratio. The theoretical density and the voids content in nanocomposites were evaluated through the rule of mixture, as detailed in our

previous work [25]. The results are the average of five measurements.

2.3.3. Thermogravimetric analysis (TGA)

Thermal degradation was performed in nitrogen flow of 10 mL/min by using a Q5000 IR thermogravimetric analyzer (TA Instruments-Waters LLC, New Castle, DE, USA). Samples of about 20 mg were tested up to 700°C at a heating rate of 10 K/min. The onset temperature of degradation (T_{onset}) was determined by the intersection point of the two tangent lines, and the maximum temperature ($T_{d,max}$) was defined by the maximum of the first derivative of weight loss. Residual weight at selected temperature was also reported.

2.3.4. Vicat softening temperature (VST)

Vicat softening temperature was evaluated by an HDT-VICAT instrument (ATS-Faar S.p.A., Segrate, Milano- Italy) according to ASTM D1525-09. Three 3D-printed specimens of 2 mm thickness were tested at a heating rate of 120 K/h under an applied load of 10 N. The results of top surface and bottom surface were compared for each composition.

2.3.5. Mechanical test

Uniaxial tensile test on 3D-printed samples was carried out by using an Instron® 5969 electromechanical tester (Norwood, MA, USA) with a load cell of 50 kN. 3D-printed specimens had a dumbbell geometry according to ISO 527 type 1BA (gauge length of 30 mm; width of 5 mm and thickness of 2 mm). Elastic modulus of 3D-printed samples was tested at a cross-head speed of 1 mm/min, and the strain was recorded by using an electrical extensometer Instron® model 2620-601 (Norwood, MA, USA) with a gauge length of 12.5 mm. Following to ISO 527 standard, the elastic modulus was evaluated as a secant value between strain levels of 0.05% and 0.25%. Yield and fracture properties were carried out at a crosshead speed of 10 mm/min as an average value of five replicates.

Creep test was investigated through a TA Instruments DMA Q800 (TA Instruments-Waters LLC, New Castle, DE, USA) at a temperature of 30.0°C for 60 minutes under the constant stress of 3.0 MPa on a 3D-printed parallelepiped sample (length of 30mm, width of 5 mm and thickness of 0.6 mm) with the adopted gauge length of 10.0 mm.

2.3.6. Electrical resistivity measurement

Resistivity was determined either in four-probes or in two-probes contact method.

In the first case, the test was performed on filaments (1.75 mm diameter; 30 mm length) and 3D-printed specimens (i.e. 30 × 5 × 2 mm³ and 1BA with a thickness of 0.2 mm) by using a four-probes contact configuration, according to ASTM D4496-04 standard for moderately conductive materials, as illustrated in Fig. 6(a). A voltage of 5 V was applied by a DC power supply (IPS303DD produced by ISO-TECH) between external electrodes on the samples, and then the current flow was recorded through an ISO-TECH IDM 67 Pocket Multimeter electrometer (measure of Ampere and Voltage between external electrodes and the internal electrodes, respectively).
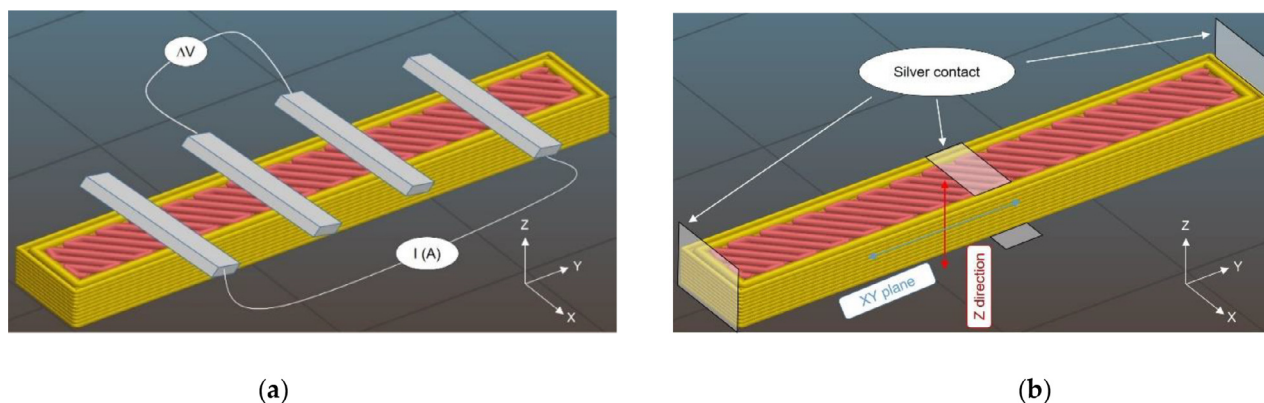
(**a**)

(**b**)

Fig. 6. Schematic illustration of resistivity measurement: (a) four-probes method and (b) two-probes method.

Table 4
Dimension and linear density of various extrudates produced from ABS and its nanocomposites, i.e. filaments (from single screw extruder), fibers and skirt (from 3D printing). Orientation factors *OF* and draw ratio *DR* during 3D extrusion calculated according to Equations 1 - 5.

Samples	Filament diameter (mm)	Fibers diameter (μm)	Skirt** diameter (μm)	Filament linear density (tex)	Fiber linear density (tex)	Skirt linear density (tex)	Feeding OF_{Feed}	Spinning OF_{Spin}	Swelling SW_{Spin}	Total OF_{Tot}	DR_{Spin}
ABS*	1725 ± 14	648 ± 21	//	2433	343	//	18.6	0.38	2.6	7.1	//
M5	1772 ± 13	450 ± 1	275	2637	170	63	19.6	0.79	1.3	15.5	2.7
M7.5	1783 ± 7	448 ± 2	274	2704	171	64	19.9	0.80	1.3	15.9	2.7
M10	1782 ± 31	424 ± 3	281	2739	155	68	19.9	0.89	1.1	17.6	2.3
S5	1744 ± 16	419 ± 3	282	2543	147	66	19.0	0.91	1.1	17.3	2.2
S7.5	1795 ± 1	410 ± 2	271	2725	142	62	20.1	0.95	1.1	19.2	2.3
S10	1779 ± 10	396 ± 5	277	2710	134	66	19.8	1.02	1.0	20.2	2.0

*comparative ABS filaments and fibers were extruded at 250°C
**equivalent diameter calculated from the skirt section

In the case of the two-probes contact method, the in-plane (XY-plane) and the through-thickness (Z-direction) electrical resistivity of 3D-printed samples were determined using a rectangle cross-section of 5 × 2 mm² and 30 mm length, and 5 × 4 mm² and 2 mm length, respectively, as schemed in Fig. 6(b). Conductive silver paint was applied on the surfaces of samples for XY-plane and Z-direction resistivity determination; then, two probe electrical resistance measurements were performed by using ISO-TECH IDM 67 Pocket Multimeter electrometer.

The electrical volume resistivity of the samples, ρ, was determined as follows:

$$\rho = R \cdot \frac{A}{L} \qquad (6)$$

where R is the experimental volume resistance, A and L are the cross-section area and the length of the specimen. The results represent the average of at least three specimens for each composition.

3. Results and discussion

3.1. Processing evaluation and morphological analysis of 3D-Printed Parts

In order to evaluate some differences, if any, between ABS and CNT nanocomposites, comparative diameters, linear density and orientation factor of filaments, fibers and skirt have been considered, as detailed in Table 4. The orientation factor during feeding is 18.6 for the matrix ABS, and about 20 for ABS/CNT, almost independently on the type of filler. On the other hand the higher the filler content, the lower the diameter freely extruded fiber, indicating an effect of polymer chain alignment and stabilization in geometry. It is evident the effect of the type of CNT,

resulting an average diameter of 441 ± 14 and 408 ± 12 μm for ABS/MWCNT and ABS/SWCNT, respectively. The orientation factor during 3D spinning (OF$_{Spin}$) is very low for ABS (about 0.4), and quite low for ABS/MWCNT (0.8 - 0.9); and in the range 0.9 - 1.0 for ABS/SWCNT. Correspondingly, the total orientation factor (OF$_{Tot}$) increased with the content of CNT, and the higher values were obtained in ABS/SWCNT nanocomposites, as consequence of a easier alignment of SWCNT with respect to MWCNT. In the same time it is also possibile to evaluate the effect of swelling during 3D extrusion; the swelling ratio (SW$_{Spin}$) is quite high for the pure matrix ABS (2.6), and it is reduced in the range 1.1 - 1.3 for ABS/MWCNT. On the contrary, SWCNT nanocomposite do not show significant swelling, as consequence of the stabilizing and homogeneous distribution of the filler along the extruded fiber.

Moreover, the different effect of CNT in fiber deposition during 3D-extrusion is evidenced by the extrusion drawing, with a higher draw ratio for ABS/MWCNT (range 2.3 - 2.7) with respect to ABS/SWCNT (range 2.0 - 2.3), for the analogous reasons of the swelling ratio.

The quality of the material continuity, the interlayer adhesion and the filler dispersion was evaluated by morphological analysis. At this purpose, the most significant scanning electron micrographs of fracture surfaces of 3D-printed samples (ten layers) of ABS/MWCNT and ABS/SWCNT composition are represented in Figs. 7 and 8, respectively. It is still well evident in the fracture surface of MWCNT at 7.5% and 10% by wt. (Fig. 7 (a, c)) the presence of filament with a quite definite semicircular section and discontinuity, especially in the external deposited filaments with the lack of good adhesion, either in the plane XY (inner), or in vertical direction (interlayer contact). On the other hand, in SWCNT 3D printed nanocomposites a higher level of interaction and adhesion between the layer and the contiguous filament are well documented. The difference could be directly attributed to the higher
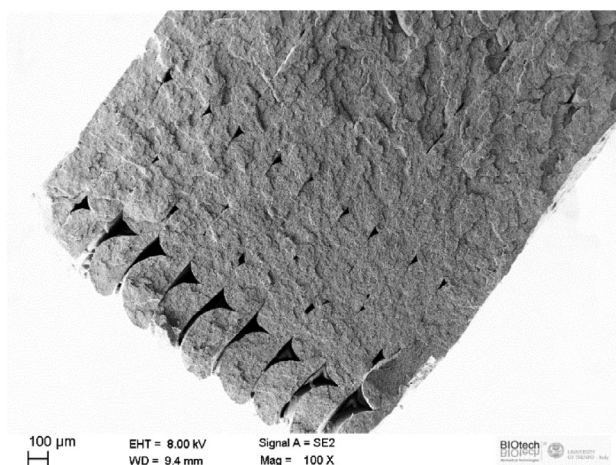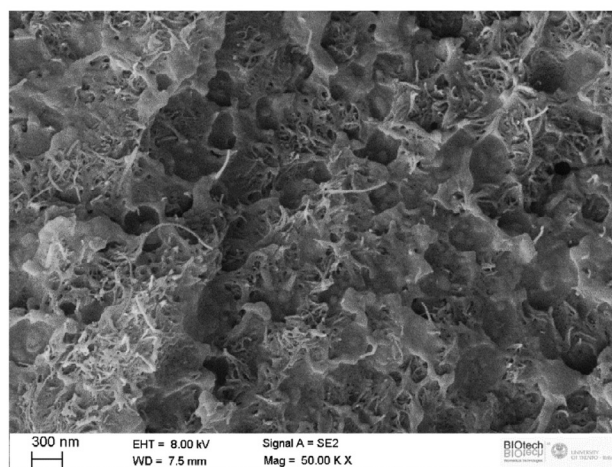
(a)
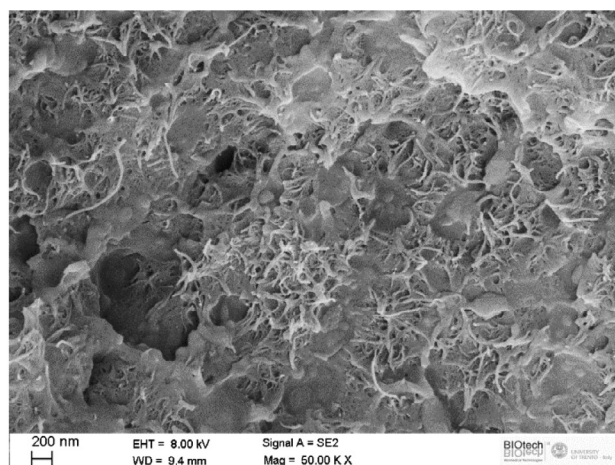
(b)
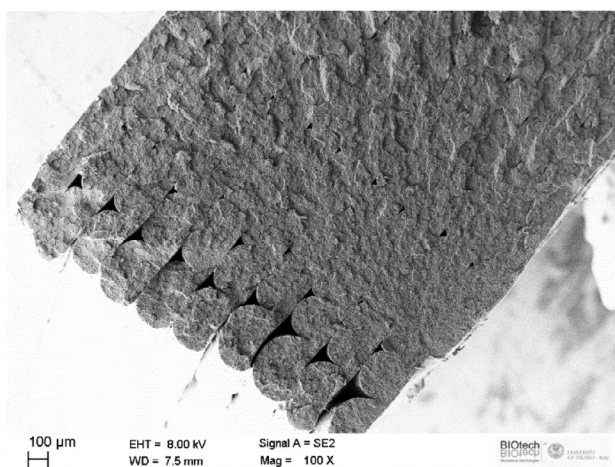
(c)

(d)

Fig. 7. FESEM micrographs of ABS/MWCNT composites: M7-3D (a - b) and M10-3D samples (c - d).

viscosity of MWCNT, in fact melt flow was found to be about 15-18 times lower than that of SWCNT [19].

Moreover, at low and high magnifications the presence of voids was observed in 3D-printed specimens. In Fig. 7(**b, d**), MWCNT were clearly observed in the SEM micrographs with uniform distribution and good dispersion. On the other hand, Fig. 8(**b, d**) revealed that the long fiber of SWCNT randomly oriented and root-like hierarchic network could be observed.

3.2. Apparent density

The apparent density of both ABS/CNT 3D-printed samples is reported in Table 5. The density of pure ABS bulk is 1.043 g/cm^3, which is consistent with the reported value in the material's technical datasheet. Density of both ABS/CNT nanocomposites in the range of 0.98 - 1.01 g/cm^3 and the void content of 6 - 8 vol.% were obtained regardless rising fraction of CNT with no specific difference between MW and SW carbon nanotubes.

3.3. Vicat softening temperature (VST) and thermal properties

The maximum Using Temperature was determined by the Vicat test performed on 3D printed plates. Vicat Softening Temper-

Table 5

Composition of 3D printed ABS and its nanocomposites (in percentage by wt. %). Density and a void fraction (V_v) as a function of CNT content.

Samples	CNT vol. (%)	Apparent density (g/cm^3)	Theoretical density (g/cm^3)	V_V (%)
ABS-3D	0.00	0.98 ± 0.01	1.041	6.2 ± 0.9
M5-3D	2.48	1.00 ± 0.01	1.069	6.3 ± 0.9
M7.5-3D	3.78	0.99 ± 0.01	1.083	8.8 ± 1.0
M10-3D	5.10	1.01 ± 0.01	1.098	8.3 ± 1.0
S5-3D	2.84	0.98 ± 0.01	1.065	8.4 ± 1.0
S7.5-3D	4.30	0.99 ± 0.01	1.077	7.7 ± 1.0
S10-3D	5.80	0.99 ± 0.01	1.090	8.8 ± 0.6

ature (VST) provides useful data of the materials rigidity at high temperature on both surfaces of the produced composite specimens (see Table 6). Representative curves of tip penetration are shown in Fig. 9. VST value progressively increased with both CNT content in the polymer matrix, indicating a continuing using temperature at least up to 90°C, and even higher. It is clearly evident that addition of SWCNT resulted in nanocomposite with a higher VST than MWCNT nanocomposites. In particular, VST was increased from about 111°C of ABS to 118°C for nanocomposites containing 10
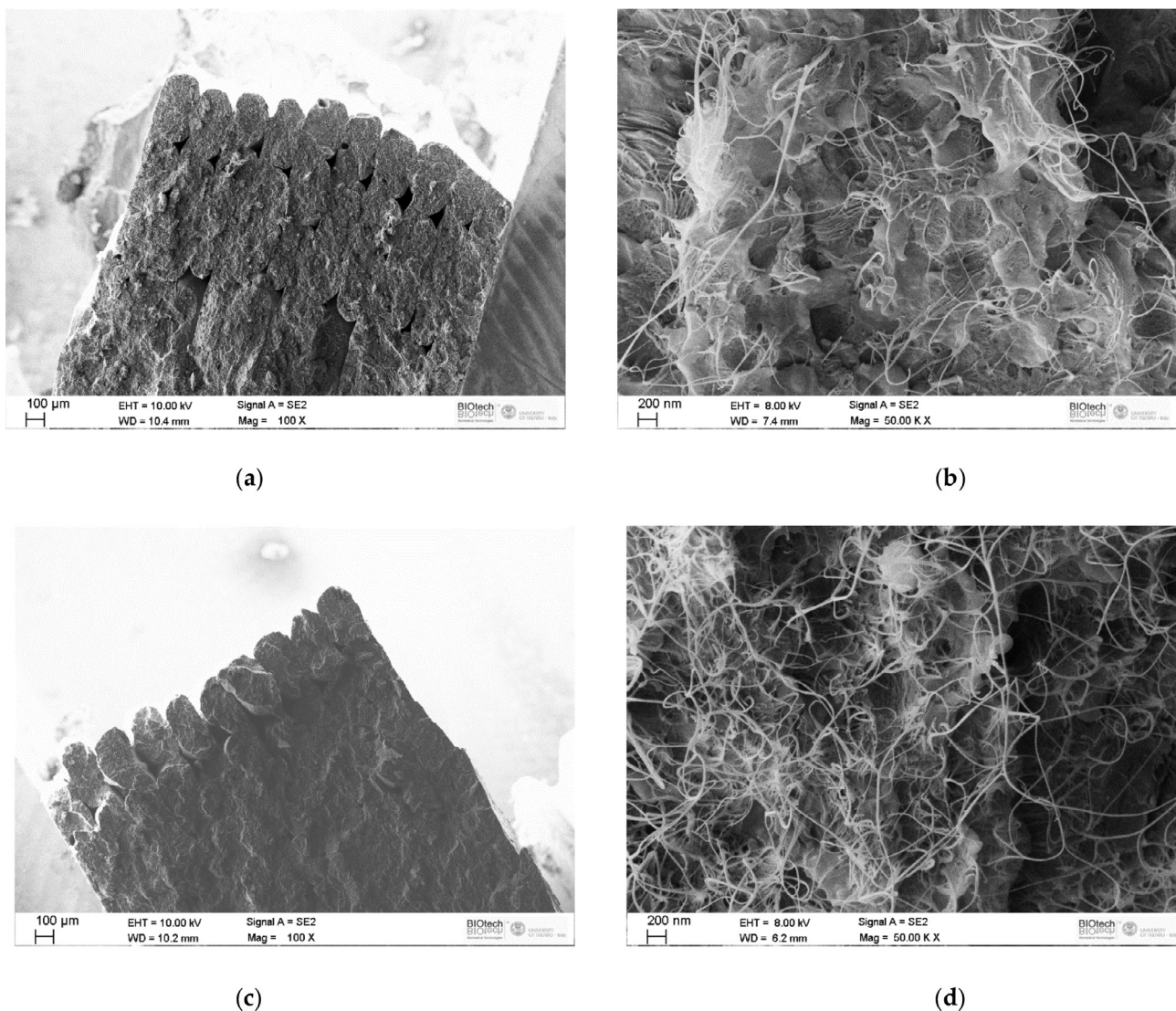
(a)

(b)

(c)

(d)

Fig. 8. FESEM micrographs of ABS/SWCNT composites: S7 - 3D (a-b) and S10-3D (c - d).

Table 6
Vicat Softening Temperature (VST) of ABS and its nanocomposites as a function of wt. % composition.

Samples	CNT vol. (%)	VST_{Top} (°C)	VST_{Bottom} (°C)	T_g* (°C)	VST -T_g** (°C)
ABS-3D	0.00	111.9 ± 0.7	110.9 ± 0.7	107.1	4.4
M5-3D	2.48	114.4 ± 0.7	114.2 ± 1.0	109.1	5.3
M7.5-3D	3.78	114.4 ± 1.0	113.8 ± 1.0	109.1	5.1
M10-3D	5.10	118.6 ± 1.1	117.4 ± 0.3	109.7	8.3
S5-3D	2.84	123.2 ± 0.8	121.7 ± 1.4	109.5	13.0
S7.5-3D	4.30	126.7 ± 0.3	125.5 ± 1.4	109.5	16.7
S10-3D	5.80	129.4 ± 1.4	129.0 ± 1.3	108.8	20.4

*average value of Tg measured in the first and second DSC scan (from reference 22)
**difference between average VST and average Tg

wt.% of MWCNT (i.e. 5%), whereas in the case of 10 wt.% of SWCNT, a corresponding value is 129°C (i.e. 17%).

No significant difference between the upper and lower surface of the 3D-printed neat ABS and its nanocomposites was observed, which is attributed to the amorphous polymer that is not sensitive to the thermal history in cooling. At the same time, VST of 3D samples has been compared to the T_g of material, that is not specifically modified by the addition of CNT, as reported in Table 6.

All VST are higher than T_g of correspondent material, and it is clearly evident the role of filler in stabilizing the amorphous matrix

in the zone of glassy-rubber transition. In particular, near softening temperature CNTs behave as stiffening agents that reduce the mobility of polymer chains, and hence an increase of VST has been observed. The higher the content of filler the higher the difference between VST and T_g. The effect of MWCNT is relatively mild (with differences of about 5-8°C), whereas increase in the range of 13 - 20°C was observed for SWCNT nanocomposite. The thermal stability and degradation of CNT-ABS composites has been widely reported in the scientific literature. Thermal stability of the produced filaments with ABS and nanocomposite at various content of

Table 7
TGA data of pure 3D-printed nanocomposite in a nitrogen atmosphere.

Samples	Mass Loss (%) at 280°C	T_{onset} (°C)	$T_{d,max}$ (°C)	MMLR (%/°C)	Residue (%) at 475°C	at 575°C	at 700°C
ABS-3D	0.52	414.6	433.3	2.15	2.8	0.6	0.0
M5-3D	0.55	412.7	435.2	1.77	10.7	6.5	6.0
M7.5-3D	0.27	412.3	433.3	1.73	13.4	9.3	9.0
M10-3D	0.48	409.2	430.2	1.64	15.2	11.7	11.4
S5-3D	0.35	412.7	436.0	1.77	11.5	7.5	7.1
S7.5-3D	0.62	415.7	435.8	1.78	13.5	9.6	9.3
S10-3D	0.37	407.5	432.5	1.70	16.0	12.5	12.2
MWCNT	-	-	-	-	96.4	95.6	94.1
SWCNT	-	-	-	-	96.2	95.5	94.5

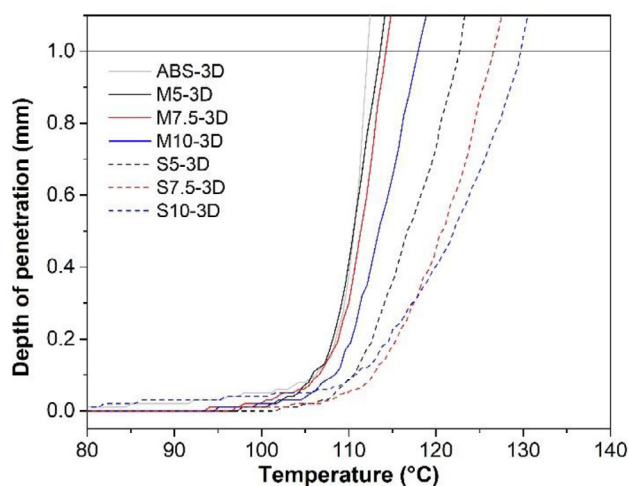MMLR: maximum mass loss rate.

Fig. 9. Vicat thermograms of tip penetration in 3D printed ABS/CNT nanocomposites – upper surface. (load 10 N; heating rate 2°C/min).

SWCNT and MWCNT were investigated by using thermal gravimetric analysis (TGA). Fig. 10 depicts the TGA thermogram of ABS/CNT-filled 3D-printed composites, while the most important parameters are summarized in Table 7.

Either ABS and ABS/CNT nanocomposites decomposed in one single step of degradation in an inert (nitrogen) atmosphere, evidencing an analogous behaviour of the butadiene and the styrenic-acrylonitrile domains in the ABS structure.

As reported in Table 7, it is firstly worth noting the almost neglectable mass loss at 280°C of 3D printed specimens (about 0.3 - 0.6%), up to three times lower than that of filaments, [22], evidencing a good thermal stability of nanocomposite products after FFF. Moreover, the onset temperature (T_{onset}) and maximum degradation temperature ($T_{d, max}$) show a light tendency to decrease with increasing CNT content. In addition, $T_{d, max}$ of ABS/MWCNT composites is slightly higher than that of ABS/SWCNT composites. This behaviour could be induced by the different thermal degradation of carbon nanotubes and their interaction with the thermoplastic matrix. In particular, as the concentration of CNT in ABS increases, the maximum mass loss rate (MMLR) is progressively reduced, as a direct consequence of the lower effective degradable fraction. This behavior was also observed in ABS-carbon nanotube and polypropylene-graphene composites. SWCNT has a higher aspect ratio and surface area than MWCNT. The high surface area of SWCNT reduces the value of MMLR, which is expected as a result of stronger interphase bonding between the matrix and the nanotubes. In addition, the relative char residue of ABS composite in Table 7. increases proportionally with the amount of nanofiller up

to 11.4 - 12.2% at 700°C, which is approximately 2% higher than the initial filament content. Moreover, it is possible to attribute the higher residue in the char at 700°C to the extra-char on ABS degradation. due to CNT effect that seem to stabilize the by-products of ABS thermolysis.

3.4. Tensile properties

The reinforcement effect of MWCNT and SWCNT in ABS nanocomposites is investigated on 3D-printed samples. The addition of CNT in ABS determined a stiffening effect, an increase of the strength and a significant reduction of deformation at break.

Stress-strain curves are reported in Fig. 11, and the tensile properties of ABS/MWCNT, and ABS/SWCNT nanocomposites are summarized in Table 8. As expected, both ABS/MWCNT and ABS/SWCNT show an enhancement of tensile properties with CNT content. In Table 8, the elastic modulus of SWCNT-based nanocomposites is higher than that of MWCNT-based nanocomposites.

For example, the elastic modulus of nanocomposite containing 10 wt. % of SWCNT was increased from 2278 MPa to 7045 MPa (i.e. 209%) whereas, in the case of 10 wt. % of MWCNT, a corresponding value is only 3213 MPa (i.e. 41%). The elastic modulus of the nanocomposites is influenced by the nanofiller properties such as their stiffness, shape and orientation and their dispersion level.

In general, several factors which could affect the tensile strength of ABS nanocomposites are included the filler/matrix interfacial adhesion, its aspect ratio and dispersion level in the matrix. Table 8 shows that the stiffness of ABS/SWCNT nanocomposites is higher than that of ABS/MWCNT nanocomposites which can be attributed to the higher aspect ratio and surface area of SWCNT with respect to MWCNT, as shown in Fig. 2. Moreover, some bending and twisting effects in the structure of the SWCNT could increase the bending stiffness of carbon nanomaterials with reduced dimension (and it can be easier realized in single-wall carbon nanotubes than in multiwall ones) [28] and prevent the detachment of SWCNT from ABS matrix. Therefore, these factors may induce a better interfacial interaction between the SWCNT and ABS matrix due to more efficiency in the load transfer from the ABS matrix to SWCNT. Consequently, tensile strength is higher for SWCNT nanocomposites. Another reason could also consider the 2-phase effect of 2D carbon nanomaterials stretching that was observed in carbon nanotubes which also could contribute to the stretching of the nanotube containing composite [29].

The Halpin-Tsai model is an empirical and simple prediction approach of the modulus of composites which takes into account the parameters such as the modulus of matrix (E_M) and filler (E_F), filler aspect ratio (ξ) and the volume fraction of filler (V_f). However, this model assumes a homogeneous dispersion of fillers and perfect interfacial adhesion between polymer/filler [30–34]. According to Halpin-Tsai model [35,36], the tensile modulus in both longitu-
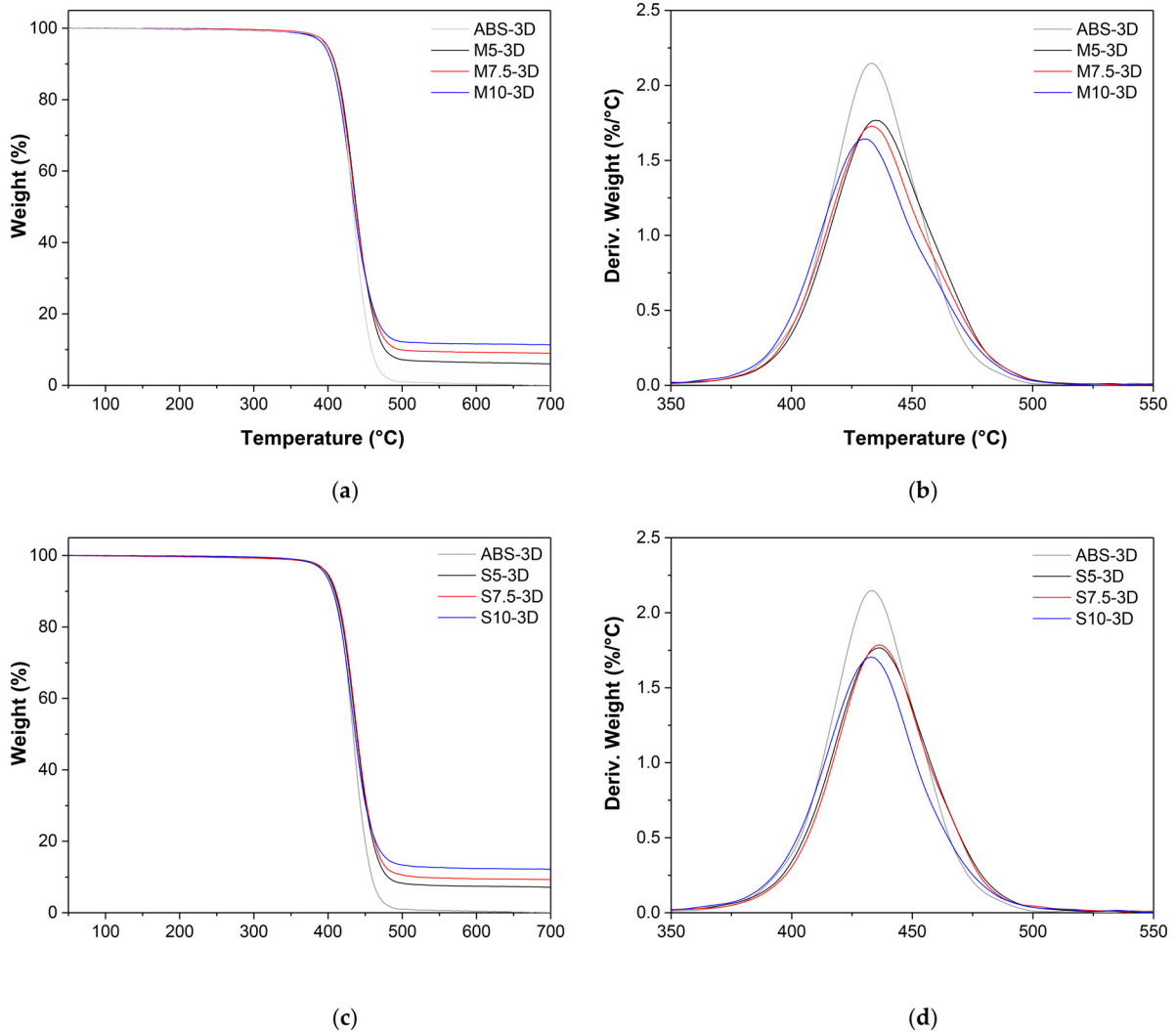
Fig. 10. TGA and DTGA curves of nanofilled ABS/MWCNT (a, b) and ABS/SWCNT (c, d) filaments under nitrogen atmosphere.

Table 8
Comparison of the tensile properties of ABS/SWCNT and ABS/MWCNT nanocomposites of 3D-printed samples.

Samples	Tensile modulus E (MPa)	Yield stress σ_y (MPa)	Yield strain ε_y (%)	Stress at break σ_b (MPa)	Elongation at break ε_b (%)	Tensile Energy to break TEB (MJ/m³)	Normalized Modulus* (--)
ABS-3D	2278 ± 118	38.0 ± 1.3	5.2 ± 0.4	31.2 ± 0.8	13.9 ± 3.1	4.09 ± 1.13	n.d.
M5-3D	2429 ± 194	42.5 ± 1.4	4.3 ± 0.2	38.4 ± 1.3	5.6 ± 0.4	1.60 ± 0.19	1.3
M7.5-3D	3119 ± 110	-	-	46.6 ± 2.6	4.2 ± 0.6	1.16 ± 0.28	4.9
M10-3D	3213 ± 13	-	-	45.0 ± 4.6	3.6 ± 0.5	0.95 ± 0.25	4.1
S5-3D	3507 ± 183	-	-	38.7 ± 3.0	2.9 ± 0.4	0.59 ± 0.11	10.8
S7.5-3D	6434 ± 254	-	-	40.5 ± 2.5	2.6 ± 0.2	0.59 ± 0.09	24.3
S10-3D	7045 ± 261	-	-	40.3 ± 2.2	1.8 ± 0.1	0.40 ± 0.03	20.9

*calculated from Eq (16)

dinal E_L and transverse E_T directions is expressed by the following equations:

$$E_L = \frac{1 + \xi \eta_L V_f}{1 - \eta_L V_f} E_M \tag{7}$$

$$E_T = \frac{1 + 2\eta_T V_f}{1 - n_T V_f} E_M \tag{8}$$

where the parameters η_L, η_T and ξ are determined as [32,37,38]:

$$\eta_L = \frac{(E_f/E_M) - 1}{(E_f/E_M) + \xi} \tag{9}$$

$$\eta_T = \frac{(E_f/E_M) - 1}{(E_f/E_M) + 2} \tag{10}$$

$$\xi = 2\frac{L_f}{D_f} \text{ forfiber} \tag{11}$$

where L_f and D_f are the length and the diameter of fibers, respectively. The volume fraction V_f is calculated to the weight fraction w_f through the following equation:

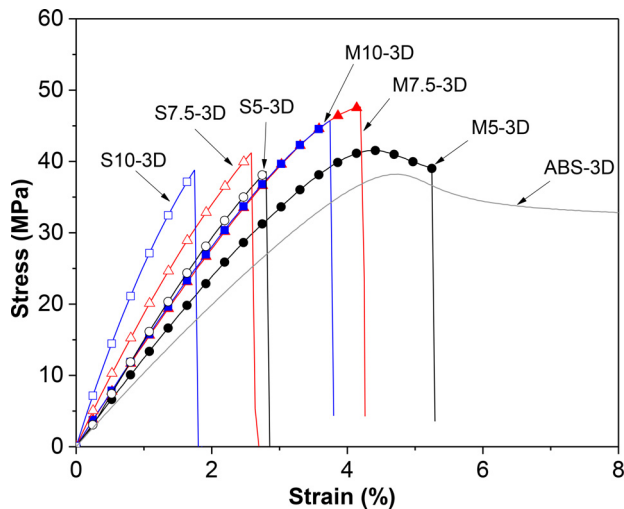$$V_f = \frac{w_f \rho_M}{w_f \rho_M + (1 - w_f)\rho_f} \tag{12}$$

Fig. 11. Representative stress-strain curves of ABS nanocomposites 3D-printed samples containing MWCNT (full symbol) and SWCNT (open symbol).

where ρ_M and ρ_f are the densities of ABS matrix and carbon nanotubes, respectively.

Consequently, three modulus of a composite can be predicted according to the literature [37 - 39]: (i) oriented fillers along the axis parallel to the loading direction (E^{Parallel}), (ii) randomly oriented fibers fillers in all two dimensional 2D-direction ($E^{\text{2D,Random}}$), and (iii) three dimensional 3D-directions ($E^{\text{3D,Random}}$).

$$E_c^{Parallel} = E_L \tag{13}$$

$$E_c^{2D,Random} = 0.375E_L + 0.625E_T \tag{14}$$

$$E_c^{3D,Random} = 0.184E_L + 0.816E_T \tag{15}$$

In this model, an experimental modulus for 3D-printed ABS of 2278 MPa was considered (Fig. 12), and the aspect ratios are considered to be equal to 158 for MWCNT ($L_f = 1500$ nm and $D_f = 9.5$ nm) and 3125 for SWCNT ($L_f = 5000$ nm and $D_f = 1.6$ nm). Elastic modulus of 70 GPa has been assumed for nanofillers (i.e. MWCNT and SWCNT) [40,41]. The experimental data are in good agreement with Halpin-Tsai model assuming a 3D randomly oriented nanofiller for ABS/MWCT composites, Fig. 12(**a**). as previously reported in literature [27].

However, the elastic moduli of ABS/SWCNT nanocomposites of the content of 2.84 vol.% (5 wt.%) fit the randomly oriented fibers fillers in all two dimensional 2D-direction, while the nanocomposite with the content of SWCNT higher than 4.3 vol.% (7.5 wt.%) is relatively higher than the parallel modulus (E^{Parallel}), as shown in Fig. 12(**b**). The underestimation of Halpin-Tsai modulus is attributed that the lower nanofiller modulus was assumed or, the less the polymer-nanoparticle interface interactions were considered [42].

Another model, Lichtenecker equation, previously suggested for the prediction of electrical properties of UHMWPE nanocomposite, [43] has been also utilized. Even if log scale allows a visible good overlapping between experimental data and fitted curves, the resulting calculated modulus of CNT are overestimated (more than 3.6 TPa), definitively higher than expected, and plots have not been reported. Following these comparative analyses, Halpin Tsai model clearly appears the more indicated for evaluation and interpretation of the different effect of orientation in CNTs, resulting 3D random in MWCNT, and parallel orientation in SWCNT.

Furtherly, to compare the mechanical properties of 3D printed ABS composites with respect to literature data, a normalized mod-

ulus, E_{norm}, was also evaluated as follows:

$$\text{Normalized modulus} = E_{norm} = \frac{E_c - E_i}{E_i w_f} \tag{16}$$

where E_c is the modulus of composite; E_i is the matrix modulus (neat ABS), and w_f is the weight fraction of incorporated filler [6,24]. Fig. 13 shows comparative results of effect of various fillers (carbon fiber CF, reduced graphene oxide r-GO, graphene nanoplatelets GNP and CNT) and the higher values of SWCNT nanocomposites are evident, close to the normalized modulus of CF nanocomposites. It is worth noting that addition of CF in percentage of about 13 wt.% - 15 wt.% allowed to obtain 3D-printed products with normalized modulus in the range 10 - 25, whereas 3D-printed ABS/SWCNT nanocomposites evidenced values of E_{norm} between 11 and 24, after addition of 5 wt.% - 10 wt.% of reinforcement.

3.5. Creep stability

The isothermal creep compliance of 3D-printed ABS/MWCNT and ABS/SWCNT composites under the constant stress of 3.0 MPa to 30°C is presented in Fig. 14. In absence of plastic deformation, as in this case, the compliance of isothermal tensile creep, $D_{\text{tot}(t)}$, is contributed by two components: elastic (instantaneous) D_{el} and viscoelastic (time-dependent) D_{ve}, as defined in Eq. (17).

$$D_{tot}(t) = D_{el} + D_{ve}(t) \tag{17}$$

The results are summarized in Fig. 14. As expected, the introduction of carbon nanotubes results in a significant increase in the creep stability of the materials. The high filler content is expected to reduce the creep compliance (see Fig. 14) because the nanofiller could restrict the polymeric chain mobility. Moreover, the creep compliance of SWCNT nanocomposite appeared to be significantly lower than that of reduced with respect to MWCNT nanocomposite at the same nanofiller content. This decrease is largely contributed to the reduction of the values of the elastic component. In summary, ABS/SWCNT nanocomposites exhibited a higher creep stability than MWCNT nanocomposites, which in agreement with an observed difference of moduli (as shown in Table 8).

Viscoelastic creep behaviour of all samples is predicted by the empirical Findley's model (power law), as shown in Eq. (18) [25,49,50]:

$$D(t) = D_e + kt^n \tag{18}$$

where D_e is the elastic (instantaneous) creep compliance, k is a coefficient related to the magnitude of the underlying retardation process and n is an exponent related to the time dependence of the creep process. The fitting parameters for experimental creep data are summarized in Table 9. The fitting model was satisfactory, as R^2 around 0.99 was found for all samples value, except S10 sample. The addition of CNT reduced the creep compliance of nanocomposites, especially in the case of SWCNT, for which both the values of parameters D_e and k resulted lower than those of MWCNT. Moreover, the coefficient n, which represents the kinetics of the flow process of macromolecules during creep time, is only marginal affected by the presence of MWCNT and SWCNT. As confirmation of the good fitting, it is also worth noting an almost equivalence of the calculated elastic component of creep, either D_{el} or D_e, obtained from Eq. 17 and Eq. 18, respectively. The lower compliance values have been shown by SWCNT nanocomposites, due to the higher orientation of reinforcement, and consequently to their higher stiffness. In fact, the higher the tensile modulus, the lower the elastic creep compliance.
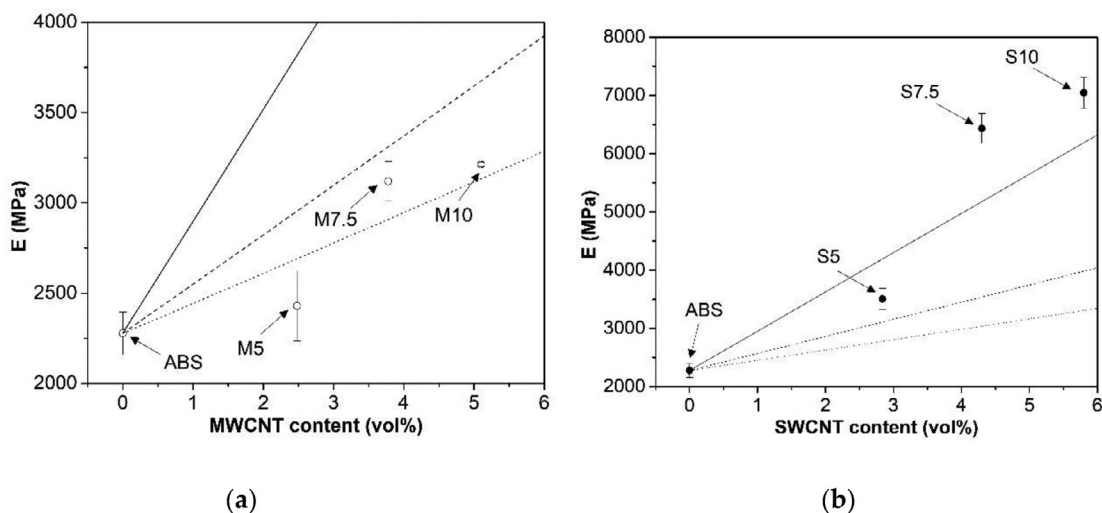
(a)   (b)

Fig. 12. Elastic modulus of nanocomposites ABS/MWCNT (a) and ABS/SWCNT (b). Continuous (___) and dash lines (_ _ _) and dot lines (…) represent prediction according to the Halpin-Tsai models with parallel, 2D random and 3D random orientation, respectively.
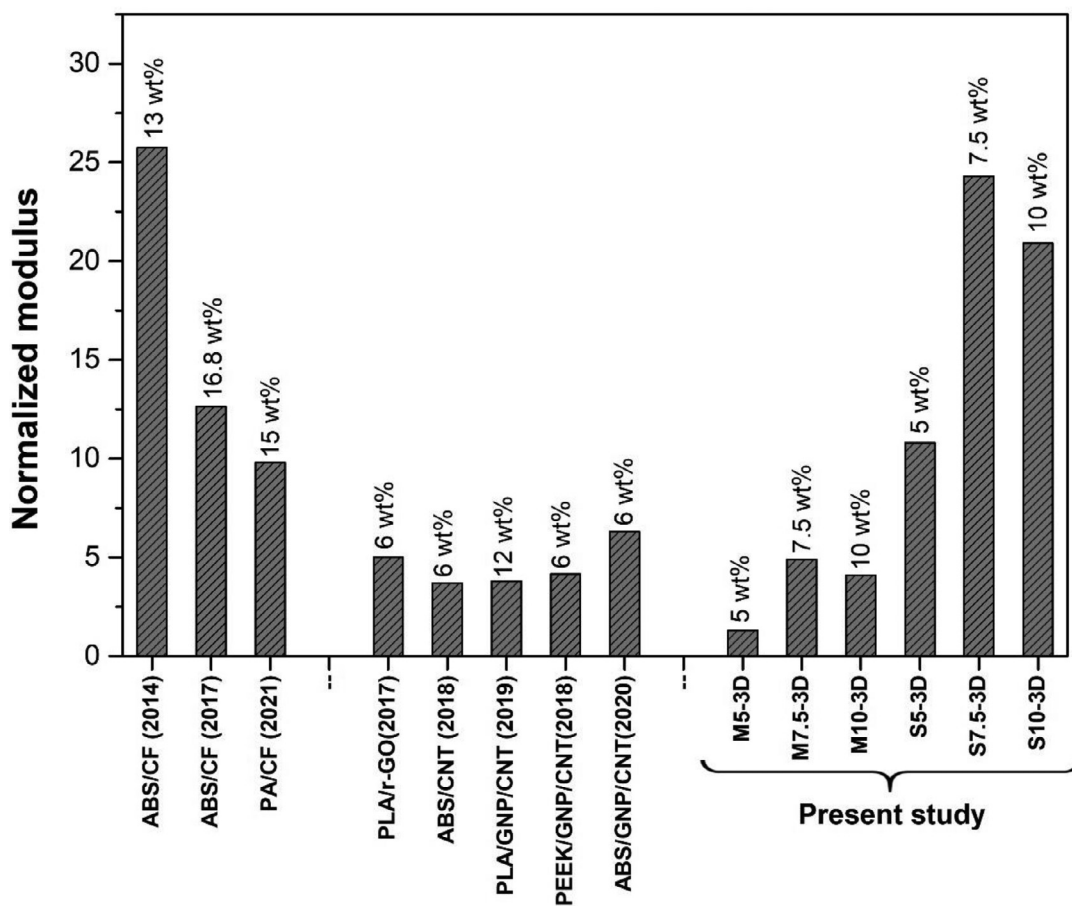

Fig. 13. Normalized modulus of 3D-printed nanocomposites, as a function of different carbonaceous wt.% content. ABS/MWCNT and ABS/SWCNT of the present study compared to literature data, such as CF in ABS [44,45] and in PA [46]; r-GO in PLA[7]; CNT in PEEK[18], PLA [47] and in ABS [25,48].

3.6. Electrical resistivity

The electrical conductivity of ABS/MWCNT and ABS/SWCNT nanocomposites was measured by four probes methods on filaments, 3D-printed on 1 layer and 10 layers within infill [± 45°] and Skirt [0°]. This was performed to clarify any plausible anisotropic electrical conductivity behavior due to the FFF 3D printing manu-

facturing technology process. Fig. 6 schematically illustrates the approach employed in carrying out the electrical conductivity. Fig. 15 shows the electrical conductivity of the 3D-printed ABS conductive nanocomposites at 5.0 wt.%, 7.5 wt.% and 10 wt.% MWCNT and SWCNT contents, respectively, on 3D-printed samples of 10 layers, 1 layer and Skirt. Skirt is the external frame of 4 aligned fibers, as shown in Fig. 5 (b, c).

Table 9

Creep test of neat ABS and its nanocomposites as measured on 3D-printed samples and fitting parameters (Equation (18)).

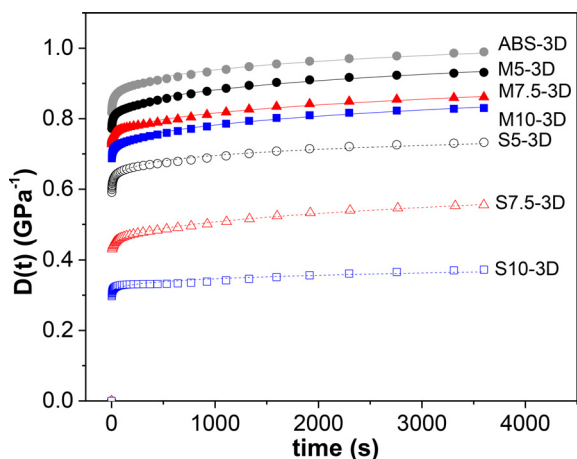| Samples	D_{el} (GPa^{-1})	$D_{ve, 3600s}$ (GPa^{-1})	$D_{tot, 3600s}$ (GPa^{-1})	D_e (GPa^{-1})	k (GPa^{-1}s^{-n})	n	R^2
ABS-3D	0.728	0.262	0.989	0.786	0.035	0.214	0.994
M5-3D	0.696	0.235	0.931	0.759	0.018	0.279	0.995
M7.5-3D	0.658	0.203	0.861	0.726	0.009	0.328	0.989
M10-3D	0.621	0.209	0.830	0.681	0.011	0.319	0.995
S5-3D	0.523	0.210	0.733	0.540	0.054	0.152	0.988
S7.5-3D	0.407	0.148	0.555	0.424	0.007	0.366	0.994
S10-3D	0.259	0.011	0.372	0.298	0.008	0.265	0.928

Fig. 14. Creep compliance, $D(t)$ of 3D-printed neat ABS, ABS/MWCNT and ABS/SWCNT samples at 3.0 MPa at a temperature of 30°C.

In Fig. 15(**a**), the resistivity of 3D-printed samples as expected, is higher than the correspondent filaments mainly due to the effects of orientation in objects produced with a raster angle ±45°, and to a partial contribute of porosity (about 6–9 vol.%). In the same time, the effect of 3D printing process for ABS/MWCNT was partially relevant in decreasing conductivity (about one order of magnitude), due to the almost 3D-random dispersion of CNT. Conversely, in the case of highly dispersed and oriented SWCNT in nanocomposite filaments, those with the lower resistivity, a much higher increase of resistivity up to two orders of magnitude was observed after 3D printing.
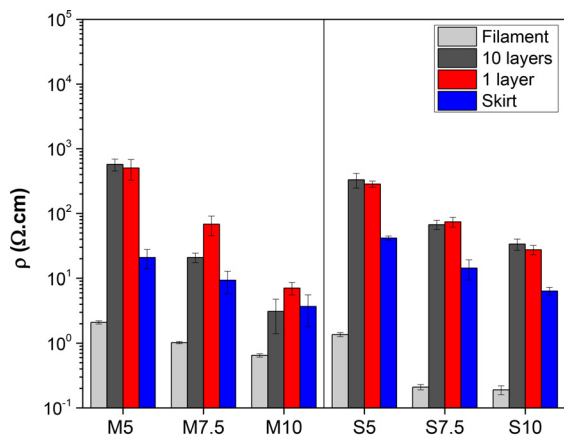
The similar resistivity of 3D-printed samples regardless of 10 layers or 1 layer, while the Skirt samples have lower resistivity due to parallel deposited printed beads.

It can be observed that for all ABS/CNT 3D-printed nanocomposites at different MWCNT and SWCNT conductive filler contents, the XY direction resistivity values were lower than the Z-direction ones, as shown in Fig. 15(**b**).

The electrical properties data suggested an anisotropic behavior of the nanocomposites, induced by the FFF process. In other words, the FFF process caused anisotropic 3D-printed parts because of the CNT orientation in the 3D printing direction and less contact of deposited fibers along the Z-direction, thus resulting in a higher electrical resistivity in the cross-layer direction. The lowest resistivity was determined for the 10 wt.% ABS nanocomposites, namely, 4.0 ± 1.7 Ω cm for the ABS/MWCNT and 10.7 ± 0.6 Ω cm for the ABS/SWCNT at the XY-direction, while that of Z-direction has 589 ± 68 Ω cm and 86 ± 12 Ω•cm for M10 and S10, respectively. Vidakis et al [12]. also reported this behaviour in the study related to FFF 3D-printed nanocomposites.

3.7. Comparisons effects of MWCNT and SWCNT

Both MWCNT and SWCNT nanocomposites filaments have been successfully used for the productions of selected geometry objects by fused filament fabrication. In order to evaluate the effect of processing on various properties of 3D products, a direct comparison of selected properties $P\%$ has been obtained according to Eq. (19), as the ratio between the property of filament, P_{Fil} from [22], and the property of 3D printed components, P_{3D},

$$P\% = 100 x P_{Fil}/P_{3D} \tag{19}$$

(a)
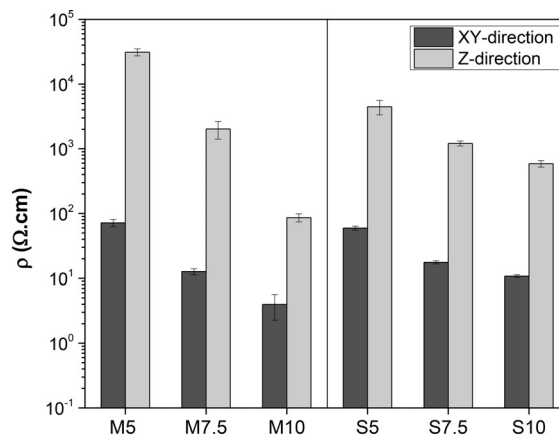
(b)

Fig. 15. Volume electrical resistivity in (Ω cm) of ABS nanocomposite of filaments, 3D-printed samples infill [± 45°] (1 layer and 10 layers) and Skirt [0°] by four-probe method (a) and 3D-printed samples infill [± 45°] 10 layers in XY-direction and Z-direction by two probe method (b).

Table 10

Comparison of relative properties of 3D-printed samples versus extruded filaments or plates (VST), as a function of MWCNT and SWCNT in ABS nanocomposites, according to Eq.19.

Samples	Tensile modulus (%)	Stress at Break (%)	Elongation at Break (%)	VST (%)	Conductivity (%)
ABS	103	89	54	100	//
M5	100	97	160	101	0.4
M7.5	120	99	127	99	4.9
M10	116	95	138	102	20.9
S5	67	74	207	102	0.4
S7.5	95	75	236	102	0.3
S10	114	74	150	98	0.6

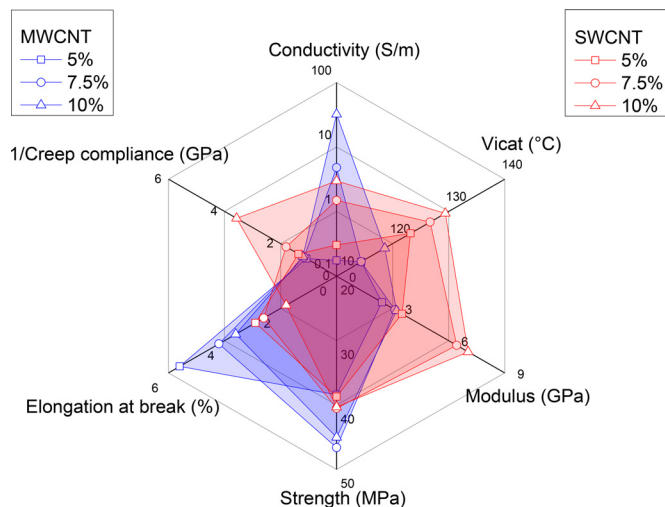*comparative data of filament; **comparative data of plate (from ref [22])

Fig. 16. Comparison of selected properties of ABS/MWCNT and ABS/SWCNT 3D-printed nanocomposites as a function of nanofiller content (5-10 wt. %).

The results are shown in Table 10. It is evident a certain reduction of properties especially in electrical properties (along main direction). Tensile modulus did not show significant variation in MWCNT nanocomposites and in 10 wt.% SWCNT nanocomposite. A progressive reduction of stress at break was observed in SWCNT nanocomposites.

On the other hand, elongation at break of nanocomposites was found to increase in 3D-printed specimens, except the case of pure matrix ABS. Vicat Softening Temperature remained almost unchanged, indicating an independence from the direction. A dramatic reduction of conductivity of 3D-printed components was observed for all SWCNT nanocomposites (0.3 - 0.6% of the initial conductivity). On the other hand, it is worth noting that 3D-products containing 7.5 and 10 wt.% MWCNT maintained about 5 and 20% of the conductivity of the pristine filaments.

Moreover, further comparative effects of MWCNT and SWCNT as nanofillers in ABS nanocomposites utilized for 3D printing could be evidenced in the radar plot, shown in Fig. 16. Conductivity, VST and mechanical properties were selected as significant and comparative reference. Fig. 16 that MWCNT determined a slight increase of the electrical conductivity; at the same time, interesting values of elongation at break and significant increase of tensile strength were observed. On the other hand, SWCNT evidenced stiffening effects (higher modulus and higher creep resistance) and a relevant increase of the Vicat softening temperature.

On the other hand, SWCNT exhibited a lower electrical conductivity, but a higher Vicat temperature; moreover, SWCNT nanocomposites revealed positive reinforcement effects on mechanical properties, such as the increase in tensile modulus but a consistent reduction of strength and strain at the break with SWCNT content.

Preliminary prototypes of thermoelectric devices have been already successfully produced by fuse filament fabrication up to twenty layers and 4 mm thick (unpublished results), confirming that these 3D printable nanocomposite could be properly utilized for the production and application up to about 90°C, and/or resistors for flexible circuits [51].

4. Conclusions

In this work, 3D-printed ABS/CNT electrically conductive polymer nanocomposite materials with enhanced mechanical properties were fabricated starting from nanocomposite filaments obtained by a double-step process, i.e. (i) melt mixing and (ii) single screw extrusion. Two different fillers with different purity degrees and nanofiller geometries, namely MWCNT and SWCNT, have been utilized at different percentages up to 10 wt.% to compare their effects on the material processing and the resulting mechanical and electrical properties. SWCNT nanocomposites evidenced a relatively easier process than MWCNT nanocomposites, due to the former's lower viscosity.

According to experimental results, both ABS/MWCNT and ABS/SWCNT 3D-printed composites confirmed better mechanical properties than simple ABS. The nanofillers determined an increase in modulus and tensile strength, as well as a certain reduction of the strain at break. The elastic modulus and tensile strength of ABS/MWCNT nanocomposite at 10 wt. % increased by 41% and 18% respectively, whereas the same mechanical properties of ABS/SWCNT nanocomposite at 10 wt.% increased by 209% (elastic modulus) and 6% (tensile strength). All the compositions of ABS/SWCNT nanocomposites showed a significant higher stiffness and higher creep resistance than ABS/MWCNT ones.

Models for modulus and creep behavior of 3D printed samples were also presented and discussed. Normalized modulus of 3D printed nanocomposites evidenced very high values for ABS/SWCNT nanocomposites, which are comparable to those of ABS/CF nanocomposites at higher carbon fiber content.

Conductivity of CNT composites was found to be dependent on the filler's content, the processing conditions and the specimens geometry. The higher the filler content, the higher the conductivity. In particular conductivity of 3D printed specimens decreased about two orders of magnitude with respects to conductivity of the feeding filaments. However, the higher the MWCNT content, the lower the decrease of conductivity. In addition, the 3D-printed nanocomposites revealed an anisotropic behavior in electrical conductivity, comparing the through-layer (XY-plane) and the cross-layer (Z-direction) printing direction, as determined by the two probes method. The best results in XY-plane were measured for 10 wt.% nanocomposites, measuring electrical resistivity of 4.0 Ω cm and 10.7 Ω cm for ABS/MWCNT and ABS/SWCNT, respectively.

The developed 3D manufactured nanocomposites having multifunctional properties positively confirm the potential applications for these ABS/MWCNT and ABS/SWCNT nanocomposites, as the

thermoelectric devices or sensors, though fabricating by 3D printer that able to make the complexity of geometries and customizability. Preliminary prototypes of thermoelectric devices have been already successfully produced by fuse filament fabrication, and new investigations will be the object of future research.

Author contributions

All authors conceptualized and designed the experiments; S.D. and B.J. performed the experiments; all authors analyzed the data and wrote the paper. All authors have read and agreed to the published version of the manuscript.

Funding

Declaration of Competing Interest

The authors declare no conflict of interest.

Acknowledgements

Supplementary materials

Supplementary material associated with this article can be found, in the online version, at doi:10.1016/j.jmst.2021.11.064.

References

[1] K.V. Wong, A. Hernandez, ISRN Mech. Eng. (2012) (2012) 30–38.
[2] S. Dul, L. Fambri, A. Pegoretti, Compos. Part A Appl. Sci. Manuf. 85 (2016) 181–191.
[3] I. Durgun, R. Ertan, Rapid Prototyp. J. 20 (2014) 228–235.
[4] S.J. Leigh, R.J. Bradley, C.P. Purssell, D.R. Billson, D.A. Hutchins, PLoS ONE 7 (2012) 49365–49371.
[5] J.T. Muth, D.M. Vogt, R.L. Truby, Y. Mengüç, D.B. Kolesky, R.J. Wood, J.A. Lewis, Adv. Mater. 26 (2014) 6307–6312.
[6] K. Sun, T.-S. Wei, B.Y. Ahn, Y.J. Seo, S.J. Dillon, J.A. Lewis, Adv. Mater. 25 (2013) 4539–4543.
[7] D. Zhang, B. Chi, B. Li, Z. Gao, Y. Du, J. Guo, J. Wei, Synth. Met. 217 (2016) 79–86.
[8] K. Chizari, M. Arjmand, Z. Liu, U. Sundararaj, D. Therriault, Mater. Today Commun. 11 (2017) 112–118.
[9] E. Ivanov, H.Xia Kotsilkova, Y. Chen, R.K. Donato, K. Donato, A.P. Godoy, R. Di Maio, C. Silvestre, S. Cimmino, Appl. Sci. 9 (2019) 1209.
[10] G. Spinelli, P. Lamberti, V. Tucci, R. Kotsilkova, S. Tabakova, R. Ivanova, P. Angelova, V. Angelov, E. Ivanov, R. Di Maio, C. Silvestre, D. Meisak, A. Paddubskaya, P. Kuzhir, Materials 11 (2018) 2256.
[11] G. Spinelli, P. Lamberti, V. Tucci, R. Kotsilkova, E. Ivanov, D. Menseidov, C. Naddeo, V. Romano, L. Guadagno, R. Adami, D. Mesisak, D. Bychanok, P. Kuzhir, Materials 12 (2019) 2369.
[12] M.Petousis N.Vidakis, L. Tzounis, E. Velidakis, N. Mountakis, S.A. Grammatikos, C. 7 (2021) 38.
[13] D. Yuan, D. Pedrazzoli, I. Manas-Zloczower, Inter. Polym. Process. 31 (2016) 554–561.
[14] J. Li, P.-S. Wong, J.-K. Kim, Mater. Sci. Eng., A 483-484 (2008) 660–663.
[15] S.Y. Yang, W.-N. Lin, Y.-L. Huang, H.-W. Tien, J.-Y. Wang, C.-C.M. Ma, S.-M. Li, Y.-S. Wang, Carbon 49 (2011) 793–803.
[16] P.-N. Wang, T.-H. Hsieh, C.-L. Chiang, M.-Y. Shen, J. Nanomater. 2015 (2015) 9.
[17] F. Daniel, N.H. Patoary, A.L. Moore, L. Weiss, A.D. Radadia, Int. J. Adv. Manuf. Tech. 99 (2018) 1215–1224.
[18] J. Gonçalves, P. Lima, B. Krause, P. Pötschke, U. Lafont, J. Gomes, C. Abreu, M. Paiva, J. Covas, Polymers 10 (2018) 925–944.
[19] S. Kumar, L.L. Sun, S. Caceres, B. Li, W. Wood, A. Perugini, R.G. Maguire, W.H. Zhong, Nanotechnology 21 (2010) 105702.
[20] P.-G. Ren, Y.-Y. Di, Q. Zhang, L. Li, H. Pang, Z.-M. Li, Macromol. Mater. Eng. 297 (2012) 437–443.
[21] H. Oxfall, G. Ariu, T. Gkourmpis, R.W. Rychwalski, M. Rigdahl, eXPRESS Polym. Lett. 9 (2015) 66–76.
[22] B.J.A. Gutierrez, S. Dul, A. Pegoretti, J. Alvarez-Quintana, L. Fambri, J. Carbon Res. 7 (2021) 33.
[23] H.K. Sezer, H.O. Eren, J. Manuf. Process. 37 (2019) 339–347.
[24] sS.P. Versalis, A sinkral® f 322- abs product data (2021) https://www.Materialdatacenter.Com/ms/en/tradenames/sinkral/versalis ±s%252ep%252ea/sinkral%c2%ae±f±332/c6da6726/1895January 18.
[25] S. Dul, L. Fambri, A. Pegoretti, Nanomaterials 9 (2018) 49–73.
[26] Graphene nanotubes tuball^tm product data (January 18, 2021) https://tuball. Com/additives/tuball/.
[27] S. Dul, A. Pegoretti, L. Fambri, Nanomaterials 8 (2018) 674–693.
[28] A.V. Savin, E.A. Korznikova, S.V. Dmitriev, Mech. Mater. 137 (2019) 103123.
[29] I. Evazzade, I.P. Lobzenko, D. Saadatmand, E.A. Korznikova, K. Zhou, B. Liu, S.V. Dmitriev, Nanotechnology 29 (2018) 215704.
[30] J. Liang, Y. Huang, L. Zhang, Y. Wang, Y. Ma, T. Guo, Y. Chen, Adv. Funct. Mater. 19 (2009) 2297–2302.
[31] J.C. Halpin, J.L. Kardos, Polym. Eng. Sci. 16 (1976) 344–352.
[32] K. Kalaitzidou, H. Fukushima, H. Miyagawa, L.T. Drzal, Polym. Eng. Sci. 47 (2007) 1796–1803.
[33] A. Duguay, J. Nader, A. Kiziltas, D. Gardner, H. Dagher, Appl. Nanosci. 4 (2014) 279–291.
[34] J.A. King, D.R. Klimek, I. Miskioglu, G.M. Odegard, J. Compos. Mater. 49 (2015) 659–668.
[35] J.C. Halpin, T.W. Tsai, in: Effects of environmental factors on composite materials, Air Force Materials Laboratory Rept, U.S, 1967, p. 423. AFML-TR-67.
[36] J.C. Halpin, J. Compos. Mater. 3 (1969) 732–734.
[37] M.A. Van Es, Polymer-clay nanocomposites: The importance of particle dimensions M.A., Delft University of Technology, 2001 Ph.D. Thesis.
[38] H.M. Chong, S.J. Hinder, A.C. Taylor, J. Mater. Sci. 51 (2016) 8764–8790.
[39] T.D. Fornes, D.R. Paul, Polymer 44 (2003) 4993–5013.
[40] M. Karevan, R.V. Pucha, M.A. Bhuiyan, K. Kalaitzidou, Carbon. Lett. 11 (2010) 325–331.
[41] D. Pedrazzoli, A. Pegoretti, J. Reinf. Plast. Compos. 33 (2014) 1682–1695.
[42] A. Dorigato, Y. Dzenis, Mech. Mater. 61 (2013) 79–90.
[43] O. Maruzhenko, Y. Mamunya, G. Boiteux, S. Pusz, U. Szeluga, Int. J. Heat Mass Transf. 138 (2019) 75–84.
[44] L.J. Love, V. Kunc, O. Rios, C.E. Duty, A.M. Elliott, B.K. Post, R.J. Smith, C.A. Blue, J. Mater. Res. 29 (2014) 1893–1898.
[45] D. Jiang, D.E. Smith, Addit. Manuf. 18 (2017) 84–94.
[46] S. Dul, L. Fambri, A. Pegoretti, J. Mater. Eng. Performance. 30 (2021) 5066–5085.
[47] R. Kotsilkova, I. Petrova-Doycheva, D. Menseidov, E. Ivanov, A. Paddubskaya, P. Kuzhir, Composi. Sci. Technol. 181 (2019) 107712.
[48] S. Dul, L.G. Ecco, A. Pegoretti, L. Fambri, Polymers 12 (2020) 101–120.
[49] G. Williams, D.C. Watts, D.C. Trans, Faraday Soc. 66 (1970) 80–85.
[50] W.N. Findley, Polym. Eng. Sci. 27 (1987) 582–585.
[51] B.J.A. Gutiérrez, L.G.N. González, J.A. Quintana, J. Mater. Sci. 56 (2021) 17112–17130.